ROYAL SOCIETY OF CHEMISTRY

PAPER

Comparative structural analysis of stereom polymorphs in the sea urchin test†

Ronald Seidel,[ab] Konrad Handrich,[a] Marie Albéric,[c] Jonathan Perrin,[d] Derk Joester, [iD][e] Yael Politi [iD] *[af] and Luca Bertinetti [iD] *[a]

The fenestrated ultrastructure of the sea urchin endoskeleton has attracted the attention of researchers in different fields due to its morphological complexity and crystallographic properties. Microscopic calcitic trabeculae form an intricate bicontinuous network, called the stereom. The stereom exhibits a wide variation of pore patterns, but is essentially a single calcite crystal (mono-crystalline). The polymorphism and crystal orientation in the skeletons of sea urchins have both been previously extensively described, mostly for taxonomical reasons and for mechanical studies. Moreover, while the resemblance of the stereom architecture to constant-mean-curvature (CMC) structures has been pointed out, a quantitative description and critical analysis is still lacking. Here, we use synchrotron micro-computed tomography to capture the three-dimensional (3D) architecture of the skeletal stereom in sea urchins for morphological quantification. By characterising the different stereom types, we define a data processing pipeline that allows inter-individual and interspecies comparison of stereom architectures, with implications for sea urchin taxonomy, mechanics, and skeletal growth. We further show that the various stereom morphologies are bicontinuous CMC surfaces that are unconstrained by crystallography. Our results highlight the properties of the soft tissue filling the stereom pore space in defining the shape of sea urchin biocalcite.

Introduction

The endoskeleton of echinoderms illustrates the sophistication of design achieved through millennia of evolutionary refinement. Made of brittle, crystalline

ᵃB CUBE - Center for Molecular Bioengineering, TUD Dresden University of Technology, Dresden, Germany. E-mail: luca.bertinetti@tu-dresden.de; yael.politi@tu-dresden.de

ᵇSection Biomedical Imaging, Molecular Imaging North Competence Center (MOINCC), Department of Radiology and Neuroradiology, University Hospital Schleswig-Holstein and Kiel University, Am Botanischen Garten 14, 24118 Kiel, Germany

ᶜSorbonne Université, CNRS, Chimie de la Matière Condensée de Paris, LCMCP, F-75005 Paris, France

ᵈSoleil Synchrotron, Science Division, Gif-sur-Yvette, France

ᵉDepartment of Materials Science and Engineering, Northwestern University, 2220 Campus Dr, Evanston, Illinois 60208, USA

ᶠCluster of Excellence Physics of Life, TUD Dresden University of Technology, Dresden, Germany

calcite (CaCO$_3$) building blocks, it provides robust mechanical support despite its porous and lightweight construction. The corona or test, a mineralized tissue that encapsulates the soft body of the sea urchin, is composed of individual plates arranged in alternating column pairs (five ambulacral and five interambulacral Fig. 1A–E).[1–3] Each interambulacral plate in regular urchins has a large primary tubercle and several smaller ones, serving as attachment sites for the spines (Fig. 1F). The coronal plates form a porous structure called stereom, a complex, bicontinuous network of calcitic trabeculae (Fig. 1F–H).[4–9] The connective tissue (stroma) pervades the complex continuous pore system and orchestrates crystal growth.[10] Connections between individual corona plates and between the spines and the tubercle are made by collagenous ligaments.[11–13]

The trabeculae of the stereom consist of crystalline magnesian calcite ((Ca$_{1-x}$Mg$_x$)CO$_3$, $x \leq 0.12$ (ref. 14)). While both the test plates and the spines in
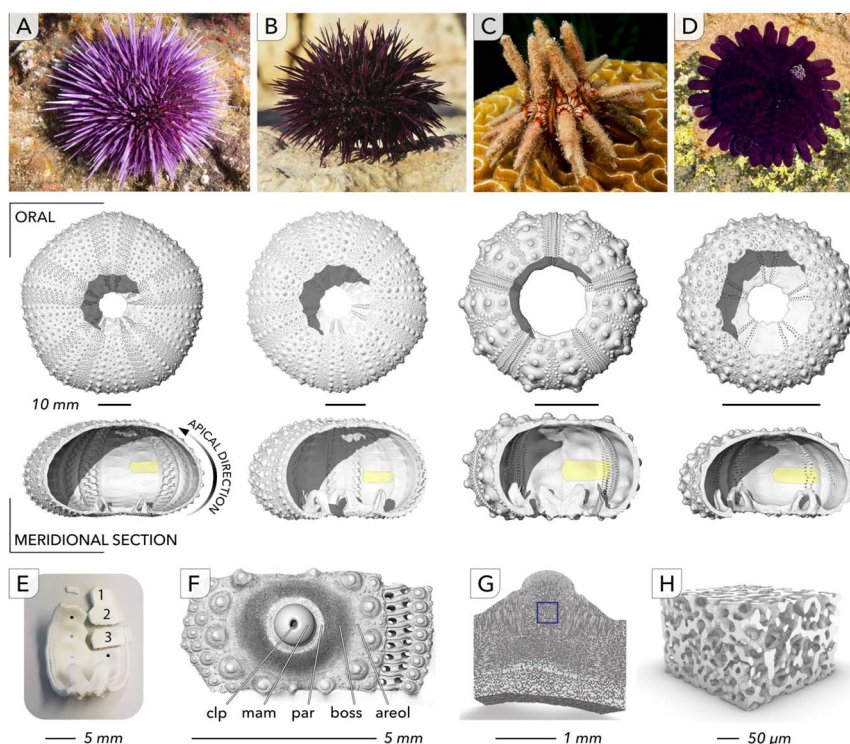

Fig. 1 (A–D) Photographs (first row) and volume renderings of μCT reconstructions of the test in ab-oral (second row) and lateral cut-away aspect (third row) of adult specimens of *Strongylocentrotus purpuratus* (column A), *Paracentrotus lividus* (B), *Eucidaris tribuloides* (C) and *Colobocentrotus atratus* (D) showing the endoskeleton is comprised of individual staggered test plates (forming ambulacral and interambulacral columns). (E) Photograph of an interambulacral column from *C. atratus*, comprising individual test plates. (F) Maximum intensity rendering of an interambulacral test plate with primary and multiple secondary tubercles on the surface serving as attachment sites for the spines. Abbrev.: clp = central ligament pit, mam = mamelon, par = parapet, boss = boss, areol = areole. (G) Cut-away rendering of SR-μCT reconstruction of a tubercle of a *S. Pur.* test plate, and (H) exemplary calcitic stereom morphotype (region highlighted by the blue square in (G)) illustrating the test plate's high porosity.

sea urchins behave like single crystals when observed under polarized light[1,15] or with X-ray and electron diffraction techniques,[7,16] around 10 wt% of the mineral remains indefinitely amorphous.[17,18] The test grows by enlargement of existing coronal plates as well as the addition of new ones.[1,3,11,19–25] In adult sea urchin spines[26,27] and larvae,[28] crystals are thought to grow by attachment of amorphous mineral precursor particles.[29–31] In the sea urchin test, a similar mechanism may allow the seamless extension of the stereom network in crystallographic continuity with the existing calcite.

The orientation of the crystallographic lattice relative to the shape of the coronal plates can vary significantly between species and even between ambulacral- and interambulacral-plates of the same species. It is commonly used as a taxonomic and phylogenetic classification tool.[1,2,7,12,32] In contrast to the bulk of the plate, the primary tubercle tip (the mamelon) is typically polycrystalline (Fig. 2).

At least 10 stereom subtypes have been described previously that differ in two characteristic properties: the relative alignment (or orientation) of trabeculae and pores, and their dimensions. This type of polymorphism (not to be confused with crystal polymorphism) is observed both between different species of sea urchins and within single test plates (Smith 1980 (ref. 5)). How the stroma controls which subtype is deposited remains poorly understood. However, the association with
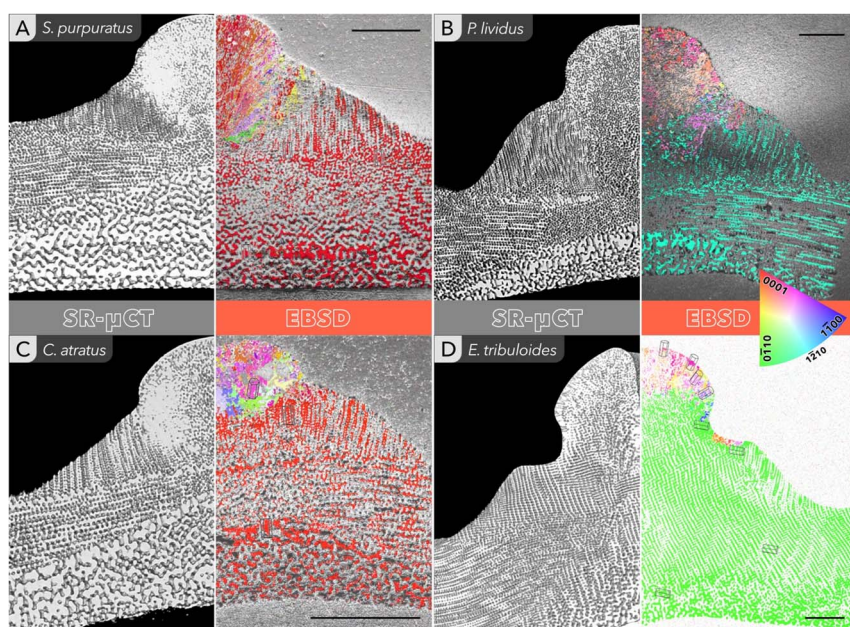

Fig. 2 ((A–D), left image) Rendering of virtual sections through binarized SR-μCT reconstructions of interambulacral test plates of *Strongylocentrotus purpuratus* (A), *Paracentrotus lividus* (B), *Colobocentrotus atratus* (C) and *Eucidaris tribuloides* (D). Note that only the left half of each section is shown. (Right image) Crystallographic orientation maps superimposed on backscattered electron images of ground-and-polished sections of interambulacral test plates. For the color key, refer to the inverse pole figure of calcite (inset). The reference direction is aligned with the y-direction of the map. Scale bars: 500 μm.

different soft tissues (*e.g.*, muscles, collagenous ligaments) and the biomineral deposition rate[21] seem to play a role. For example, fast growth results in the formation of an open meshwork with large pore space, whereas denser, more compact stereom is associated with slow growth rates.[3,9,21,33] The relative shape, size, and orientation of trabeculae and pore space are thought to serve local mechanical requirements.[34–37] Maintaining high porosity without compromising mechanical strength requires a high level of structural optimization.[38–40] It has recently been shown that the alignment of crystallographic axis and stereom lattice orientation leads to improved damage-tolerance in star-fish stereom.[36,37] These types of studies rely on three-dimensional (3D) X-ray based micro-computed tomography (μCT) measurements of stereom architectures in conjunction with finite element modelling/analysis (FEM/FEA), and would benefit from a quantitative and parameterized description of the stereom architecture.

Herein, we report on the quantitative analysis of the 3-dimensional architecture of the stereom in the test plates of four sea urchin species: *Strongylocentrotus purpuratus* (*S. pur.*), *Colobocentrotus atratus* (*C. atr.*), *Paracentrotus lividus* (*P. liv.*), and *Eucidaris tribuloides* (*E. tri.*). The crystallographic axes of calcite in the test plates vary between species. In *P. liv.* and *E. tri.*, the calcite is oriented with its *c*-axis parallel to the plate surface and along the apical direction of the complete test. In *S. pur.* and *C. atr.*, the *c*-axis is oriented perpendicular to the plane of the plate (*i.e.*, radially with respect to the test). Our primary questions are to what extent the lattice orientation is correlated with the morphological features of different stereom structures, as well as what minimal set of parameters best describes these architectures and their variability within and across different species.

We employed high-resolution synchrotron micro-computed tomography (SR-μCT) to generate 3D reconstructions of plates from the four sea urchin species cited above. Mineral and pore space were identified *via* binary thresholding. Binarized volumes were segmented to identify and classify regions within each test plate that share similar morphological features. The stereom subtypes were then quantitatively compared across species in terms of specific architectural features (*e.g.*, symmetry, porosity and branch thickness, surface area and curvatures) and alignment within the test plate as well as relative to the calcite crystal orientation. Our results demonstrate high plasticity in stereom architecture, irrespective of crystallographic orientation or symmetry, suggesting that the soft tissue exerts a large degree of control over the final shape. The robust analytical pipeline presented herein is suitable for large-scale comparative analysis of stereom structure across different echinoderms and in fact may be generalized to a broad range of materials.

Materials and methods

Specimens

The four sea urchins species (*Strongylocentrotus purpuratus*, *Paracentrotus lividus*, *Eucidaris tribuloides* and *Colobocentrotus atratus*) were chosen for this study because of the availability of complete tests from adult specimens, and of published crystallography data (*e.g.*, Raup 1959 (ref. 1)). All the intact tests were purchased from private vendors, with the exception of *P. liv.*, which was supplied by the Roscoff biological station of Sorbonne University (France). Live sea urchins

of *P. liv.* were sacrificed and cleaned of all soft tissues using 5% sodium hypo-chlorite (NaClO) solution for 6 h, before being extensively rinsed with distilled water and air-dried.

Entire skeletons (tests) were used to perform lab-based micro-tomography. Subsequently, multiple individual test plates from the interambulacral columns were carefully extracted from the largest plates, from half way between oral and aboral columnar ends, using standard metal dissection tools.

Some individual test plates were prepared for synchrotron micro-computed tomography. For EBSD experiments, other plates were embedded in EPON, cut in half (Buehler IsoMet low speed saw) and mounted on a (poly-methylmethacrylate) PMMA object slide using double-faced adhesive tape. Sections were polished with sandpaper plates with descending grain sizes (Log-itech PM5 Precision Lapping and Polishing Machine), and finally using a soft polishing plate with diamond spray (0.25 μm grain size).

Scanning electron microscopy (SEM)

We performed both electron backscatter diffraction and backscatter SEM imaging (*i.e.*, using a backscatter electron detector) on sections polished along the longi-tudinal direction with respect to the intact sea urchin test.

Electron backscatter diffraction (EBSD). Overview images were obtained at an acceleration voltage of 15 kV and source current of 1.6 nA, at 0.2 mbar H_2O pressure with point measurement step sizes ranging from 1.5 to 3 μm, chosen depending on the stereom trabecular thickness.

Backscatter electron microscopy (BSE). BSE images were acquired in back-scatter mode using a Field Emission-Environmental Scanning Electron Micro-scope (FE-ESEM, FEI Quanta 600F) in environmental mode (*i.e.*, at low vacuum without coating the samples with a conductive layer) with an acceleration voltage of 12.5–15 kV and a working distance of 7.8 mm.

X-ray tomography

Micro-computed tomography. In-house tomographic data was obtained using an EasyTom Nano 160 (RX Solutions, Chavanod, France). μ-CT scans were per-formed with whole, non-embedded skeletons, with isometric voxel sizes of 11–33 μm, at 60–80 kV source voltage and 155–280 μA source current, and a 1 mm copper filter. Multiple dry individual test plate samples were scanned at isometric voxel sizes of 1–3.5 μm, at 60–80 kV source voltage and 120–200 μA source current. Reconstructions were done with RX Solutions software.

Synchrotron radiation computed tomography (SR-μCT). Absorption contrast tomography imaging was performed at the ANATOMIX ('Advanced Nano-tomography and Imaging with coherent X rays') beamline of the Synchrotron SOLEIL facility located in Gif-sur-Yvette, France (Experiment Title: "Three-dimensional quantification of complex skeletal architectures in sea urchins", Proposal #20200811). Individual test plates were glued on object holders (with the primary axis in the vertical position). Due to the field of view and resolution dilemma, 3–4 separate scans, vertically stacked, were acquired and registered, resulting in complete 3D volume acquisition of entire test plates. Tomographic projections were gathered in half acquisition mode (180° sample rotation, Delta Tomo 1Tx = −1.2 mm) with final volumes of ∼4 × 4 × 2 mm and isometric voxel

sizes of 1.3 μm. The setting included the Orca Flash v4 revolver detector, a 5-fold objective and a 20 μm Gold filter. Reconstruction was performed on site.

Structural analysis

Fiji[41] was used to align the raw 3D volumes to a single volume containing an entire test plate. Data processing, segmentation and imaging were performed in Amira-Avizo (Thermo Fisher Scientific) using available rendering, slicing and manipulating modules as well as Dragonfly 3D World v. 2024.1. The grayscale depth of reconstructed datasets was reduced from 32 bit to 16 bit. Histogram normalisation was not necessary, as the structural information was not impacted by differences in grey values. Afterwards, segmentation was performed *via* thresholding in order to separate stereom from background (and pore space), followed by a further reduction to 8-bit pixel depth. We took voxel-based, mesh-based and skeleton-based approaches, using the segmented data to annotate domains characterised by similar stereom structures and to create both surfaces describing the topology of the structure and skeletons describing the structure's layout.

The annotation of the stereom types was performed using the python library bmmltools. For the technical details, see the ESI.†

For the analysis of the structural parameters, we developed a custom code based on the python libraries skan[42] (v. 0.11.1) for the skeletal analysis and libigl (v. 2.4.1) for the analysis of surface areas and curvatures. In order to benchmark to accuracy of the outcome of our python-based analyses, we applied two strategies: (1) performing parallel analyses in Amira and Meshlab with the same data (*e.g.*, sub-volumes > meshes > skeletons) for comparison, and (2) using 3D-parametric models of trabecular architectures of known geometry (*i.e.*, thickness of branches, number of branches and nodes) created with Rhino3D (McNeel, R. & others, 2010. Rhinoceros 3D, Version 5.5. Robert McNeel & Associates, Seattle, WA.) or custom python scripts as input data. The pairwise correlation of morphometric structural parameters was calculated using the Pearson method. The principal component analysis (PCA) analysis was performed using the scikit-learn library (v. 1.5.1), using the full single value decomposition (SVD) solver.

Results

Crystallographic orientation of calcite

We analyzed the stereom structure in four different species of sea urchins (Fig. 1, top). Coronal plates were dissected from one interambulacral column (see Fig. 1, middle). 3D reconstructions of the stereom with an isotropic voxel pitch of 1.3 μm were generated using synchrotron radiation micro-computed tomography (Fig. 1, bottom).

To map the crystallographic orientation of calcite across ground-and-polished sections of coronal plates, we used electron backscatter scanning diffraction (EBSD). As previously described,[2] the plates consist of a continuous network of mineralised trabeculae with a predominantly uniform crystallographic orientation (Fig. 2, EBSD panels).

In *S. pur.* (Fig. 2A) and *C. atr.* (Fig. 2C), the calcite *c*-axis is perpendicular to the plane of the plate and the *a*-axis is roughly aligned with the tangent to the meridians of the test (*i.e.*, perpendicular to the latitudinal suture of each plate).

We will refer to this direction as the 'apical' direction (see also Fig. 1, middle row), following the nomenclature of Raup.[1] While in both *E. tri.* (Fig. 2D) and *P. liv.* (Fig. 2B) the *c*-axis is oriented along the apical direction, in *P. liv.* it is the *a*-axis $\langle 10-10 \rangle$ and in *E. tri.* it is the $\langle 11-20 \rangle$ direction that is roughly perpendicular to the plate. In agreement with previous reports, for all species, the orientation of the *c*-axis in the mamelon is not parallel to that in the bulk of the plate.[15] Instead, it is roughly perpendicular to the hemi-spherical mamelon surface. The orientation of the *a*-axes differs between microscopic domains.

Annotation of the volumetric datasets

In contrast to the striking homogeneity of the calcite orientation across most of the test plate, the stereom structure shows high spatial heterogeneity. In all species, tomograms reveal the presence of several domains that differ in trabecular thickness, orientation, symmetry, and degree of order. Manual classification and annotation of such domains present significant challenges due to the large size of the volumes (exceeding 1500^3 voxels) and the wide distribution of orientations. When viewed from different directions (*i.e.*, by examining differently oriented tomograms), domains of the same type may appear very different and could be easily misclassified.

We avoided this problem by examining the Fourier space representation of the stereom structure. Specifically, we analyzed the 3D power spectrum (PS) of small sub-volumes ($50 \times 50 \times 50$ voxels). The PS highlights periodic distance correlations and their respective symmetries, which appear as enhanced signals along specific directions in the PS.

To automate this process, we deployed a pipeline designed for minimally supervised, unbiased classification, and segmentation of 3D textural patterns. This pipeline was implemented in Python using the bmmltools library,[43] which can be run with modest computational resources and has a minimal storage and memory requirements. The algorithmic details will be outlined in a separate publication. Briefly, a set of sub-volumes (75000) was extracted from the binarized reconstruction of each dataset. For each sub-volume, the three-dimensional power spectrum was computed using the discrete-domain Fourier transform and smoothed. This was then expanded in spherical harmonics and the coefficients were used as a feature vector comprising 10^2–10^3 scalars. A clustering algorithm was employed to group feature vectors and assign a class label to each group after dimensionality reduction. To keep a low memory imprint, a machine-learning model was trained to learn the feature vector representation of each sub-volume, using the class labels as targets. Once trained, the model was used to classify a much larger set of sub-volumes extracted from the binarized reconstructions. The labels and the coordinates of all the descriptor were employed to fully annotate the original binarized datasets.

Finally, leveraging the rotationally invariant descriptor that can be computed from the spherical harmonics coefficients,[44,45] we collapsed groups that are equivalent by rotation (as illustrated for example in virtual slices in Fig. SI1, see ESI† text for details). Across the four different species, our analysis revealed the presence of 14 distinct, rotationally invariant classes (labelled in Fig. 3A with 14 different colours), each representing a unique stereom architecture that can be differentiated from others due to differences in their morphological features.
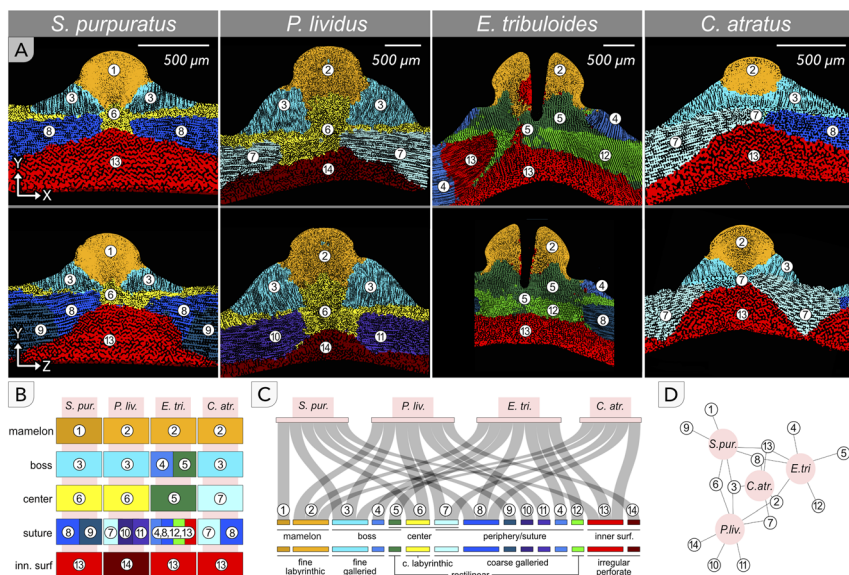
Fig. 3 (A) Virtual sections through the rotationally invariant label fields for the considered sea urchin species. Top row: Meridional virtual section. Bottom row: Circumferential section. Each color refers to a stereom structure with unique typical repeating distances, angles and symmetry. (B)–(D) Schematic diagrams summarizing the occurrence of each stereom type within and between the species.

Notably, some of these structures are common to most species studied here, while others are unique to individual species studied, as shown in Fig. 3B–D.

Classification of stereom types

Inspection of virtual slices through stereom reconstructions reveals that morphological differences between some classes are readily apparent (*e.g.*, labels 3, 6 and 13 in Fig. 3A). In others, variations in the typical distances and/or angles between trabeculae and pores are more subtle (*e.g.*, labels 7, 8 and 10 in Fig. 3A).

Grouping stereom structures that share similar 3D textural features is not straightforward when based on 2D virtual slices. However, this can be done in a simple way by examining the shape of the 3D power spectrum of representative sub-volumes. In fact, the information that is carried by the 3D power spectrum of a sub-volume is linked to both the length scale of the typical distances between trabeculae (the further apart they are in real space, the closer to the centre is the signal in the PS) and the distribution of their orientations. An isotropic signal in real space (*e.g.*, isotropically oriented trabeculae) would result in a power spectrum with spherical symmetry. A PS with reduced symmetry (*i.e.*, not isotropic) indicates the occurrence of some degree of ordering and will exhibit reduced intensity along those directions (or angular ranges) that do not have associated trabecular orientation. For example, a PS with a toroid shape would be compatible with random close packing of co-oriented cylindrical objects (all the intensity of the PS lies in one single plane, which is the one normal to the cylindrical object axis).
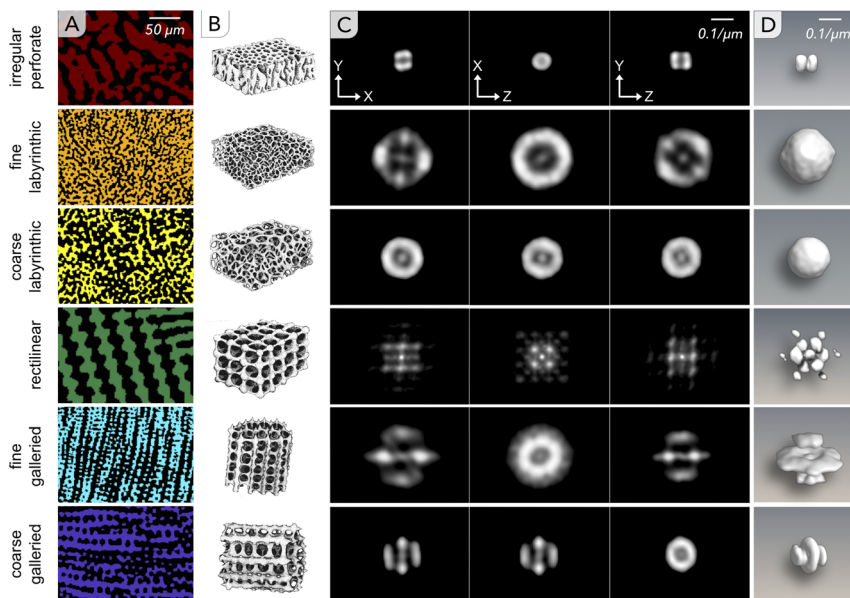
Fig. 4 (A) Virtual CT slices through representative sub-volumes for each of the identified stereom types. (B) Drawings [Smith 1980,[33] reproduced with permission] depicting the three-dimensional appearance of the different stereom types. (C) Virtual sections through the power spectra of each stereom type. The section planes are aligned normal to the principal directions of the power spectra. (D) Renderings of isosurfaces of power spectra for each stereom type.

Using this approach, we arrive at four major classes of stereom structure (depicted in Fig. 4, along with surface rendering of the respective computed power spectrum). Stereom types with similar 3D PS shape but significantly different in terms of typical distances will be referred to as subtype. The stereom types we identified in this work map onto the irregular perforate (Fig. 4 red), labyrinthic (Fig. 4, two subtypes, yellow and orange), rectilinear (Fig. 4, green) and galleried (Fig. 4, two subtypes, cyan and purple) structures described by Smith.[33] This classification was employed to assign colours/colour hues to each label in Fig. 3. Labels associated with stereom structures that vary (to a small extent) in specific dimensions and angles but exhibit the same PS symmetry will be referred to as variations of a specific stereom type or subtype and are coloured with different hues of the colour of their representative stereom type/subtype (see Fig. SI2† for examples of the PS of stereom subtypes and their variations).

It is important to emphasise that domains with very different trabecular organisation are easily annotated with different labels. Conversely, whether two domains with slightly different 3D textural features, *i.e.*, with small differences in trabecular distances and/or orientations, are annotated with the same label or not depends on the magnitude of these differences and it is determined by the sensitivity of the analysis, *i.e.*, by the choice of parameters used in the automatic segmentation pipeline.

The PS of the labyrinthic stereom is a simple hollow sphere. It is associated with a system of interconnected small pores that are randomly oriented. The pore size and distances between trabeculae vary between species. Our classification

distinguishes between coarse (Fig. 4, yellow) and fine (Fig. 4, orange) labyrinthic subtypes. The former is characterized by larger pore sizes and trabecular distances, the latter by a lower pore fraction and finer texture, where typical distances between trabeculae are around 30% smaller. Two variations of the fine labyrinthic stereom were identified (labels 1 and 2).

The PS of the galleried stereom comprises a toroid and two flanking lobes. Its lower symmetry indicates a higher degree of order. The toroid arises from the presence of parallel trabecular rods, the lobes from short, evenly spaced, and perpendicular struts[33] that interconnect the main rods. Again, we differentiate between coarse (Fig. 4, purple) and fine (Fig. 4, cyan) subtypes. Essentially, the fine subtype is a down-scaled version of the coarse one in which the spacing and thickness of trabeculae and pores are "shrunk" by up to 40%. We identified six variations of coarse galleried stereom (labels 4, 7–11).

The rectilinear stereom (Fig. 4D, green) exhibits a PS with a regular spot pattern that indicates that trabeculae form a rectilinear lattice and is found in 2 different variations (labels 5 and 12).

Finally, we identified a stereom type with a characteristic PS comprising two parallel toroids (Fig. 4, red) at relatively low spatial frequencies, corresponding to significantly thicker trabeculae and wider pores than in any of the other stereom types. Notably, stereom with comparable geometrical properties and located within the same region of the plates (see below) has been previously classified as labyrinthic. This implies that the orientation distribution of trabeculae and pores is isotropic. At least for the species considered in this work, this is not the case, as apparent from the lack of spherical symmetry in the associated PS shape. Given the thickness of the trabeculae and its reduced degree of order with respect to the regular perforate stereom,[5] we classify this stereom type as irregular perforate. We identified two different variations of the irregular perforate stereom (labels 13 and 14).

Occurrence of the different stereom types across species

Inspection of fully annotated datasets revealed that the coronal plates of each species comprise 5–7 stereom subtypes (Fig. 3). The labyrinthic and perforate stereom types are common to all species and are also localized in comparable regions. The fine labyrinthic stereom (orange, labels 1 and 2) is typically associated with the mamelon, *i.e.*, the polycrystalline region, whereas the irregular perforate stereom (shades of red, labels 13 and 14) comprises the innermost layer of the plate. A characteristic feature of the boss region in most species is the presence of a fine galleried stereom (cyan, label 3) with the main trabeculae aligned parallel to the tubercle axis. However, in *E. tri.*, this is replaced by a coarse galleried stereom (blue, label 4) sharing the same orientation of the main trabecular rods. The centre and outer regions of the plates are, in all species, typically composed of coarse galleried stereom (shades of blue, label 4, 7–11) with the main trabecular rods oriented parallel to the plate surfaces. This is present either on its own (in *C. atr.*) or in combination with labyrinthic stereom (yellow, label 6, in *P. liv.* and *S. pur.*). When coarse labyrinthic stereom is present, it is found in the core of the tubercle and its outer base, the areole. Notably, among the investigated species, *E. tri.* is distinct because most of the centre and outer regions of its test plate comprise rectilinear stereom (shades of green, labels 5 and 12).

Our findings regarding the spatial distribution of stereom types across test plates are in good agreement with prior results.[33,46] In addition, the quantitative analysis carried out here highlights commonalities and differences in stereom types both within and across species (see Fig. 3B–D).

The fine labyrinthic stereom is the most common structure between species. The fine galleried stereom is found to be consistent in shape and dimensions in almost all species, independent of the underlying crystal orientation. The one exception is seen in *E. tri.*, where the fine galleried stereom is replaced by a coarse galleried stereom. The orientation of the main trabecular rods is nonetheless similar in this region between all species.

The coarse labyrinthic stereom is found as a single structure and is only present in *S. pur.* and *C. atr.* (species sharing the same calcite lattice orientation).

The irregular perforate stereom is common to all species, but it comes in two different variations: one form superficially resembling a labyrinthic stereom but with much thicker trabeculae in *E. tri.* and *P. liv.*, or with trabeculae running at specific distances and directions in *C. atr.* and *S. pur.* (again, species sharing the same calcite orientation). In the future, a systematic analysis based on the method we describe herein could reveal whether the occurrence and the structural features of the coarse labyrinthic and the irregular perforate stereom types are linked to the underlying crystallographic orientation of calcite.

Finally, the stereom subtype with the largest number of variations is the coarse galleried (shades of blue in Fig. 3). In this case, two structures are found to be common to several species (label 7 in *P. liv.* and *C. atr.* and label 8 in *S. pur.*, *E. tri.* and *C. atr.*). Notably, each species exhibits at least two coarse galleried stereom variations. In both, the main struts align with the main in-plane axes of the plates (*i.e.*, the apical and equatorial directions of the test). However, they slightly differ in (1) the characteristic distances across and along the main trabecular rod directions and (2) the orientation distribution of the trabeculae.

These systematic differences could reflect the different loading conditions of the plate in the equatorial and meridional directions, or differences in lifestyle, habitat, and mechanical requirements (*e.g.*, in shallow water with a steady current *vs.* a rocky shelf facing high-impact waves). Furthermore, they could be related to the directional mechanical properties imposed by the underlying orientation of calcite. This seems to be the case, for example, in the ossicles of starfish where mechanical isotropy arises from the compensation between the calcite lattice properties and stereom level architectures.[47]

Morphometric analysis of stereom types

The automatic segmentation pipeline allowed us to rapidly identify and then map stereom subtypes across entire coronal plates of multiple species. This analysis is unbiased in the sense that it is not based on any *a priori* knowledge of the geometrical and morphological features of these subtypes. It is straightforward to extract metrics such as trabecular length and thickness, surface area, mineral volume fraction, or connectivity between the trabecular nodes for each subtype in a second step and perform a complete structural analysis of the stereom structures (for a complete list of descriptors considered in this study, see the ESI†). Because these metrics are based on sub-volumes rather than on 2D scanning electron micrographs or stereo views of the plates,[5,46] we expect them to be more representative. For the

following analysis, descriptors were calculated for volumes with identical size for each of the six major stereom subtypes and every species in which we observed them.

We initially considered a large set of morphometrical descriptors. For further analysis, we selected those that were not correlated with each other and some with non-trivial correlations (see the ESI† text for details). Consistent with a prior report based on 2D data,[46] some descriptors were highly correlated (Fig. 5A). The trabecular thickness (tth) and length (tl, Fig. 5C) and the mean curvature (mc) and the volume fraction (vf, Fig. 5D) are strongly positively and linearly correlated, whereas the number density of trabecular junctions (nj) is strongly negatively correlated with both the gaussian curvature (gc, Fig. 5E) and the trabecular length (Fig. 5F). We also note that the gaussian curvature is negative for all the identified stereom types and that the mean curvature is close to 0 (excluding the fine labyrinthic stereom, it varies between around -0.05 µm^{-1} to 0.05 µm^{-1}).

Principal component analysis taking into account only one descriptor for each strongly correlated pair reveals that, at least when projected onto the plane of the first two principal components (which together explain 87% of the sample variance), there is significant overlap between the stereom subtypes we identified. This indicates that the descriptors on their own do not capture all the relevant stereom features. Despite this partial overlap, the PCA points to characteristic
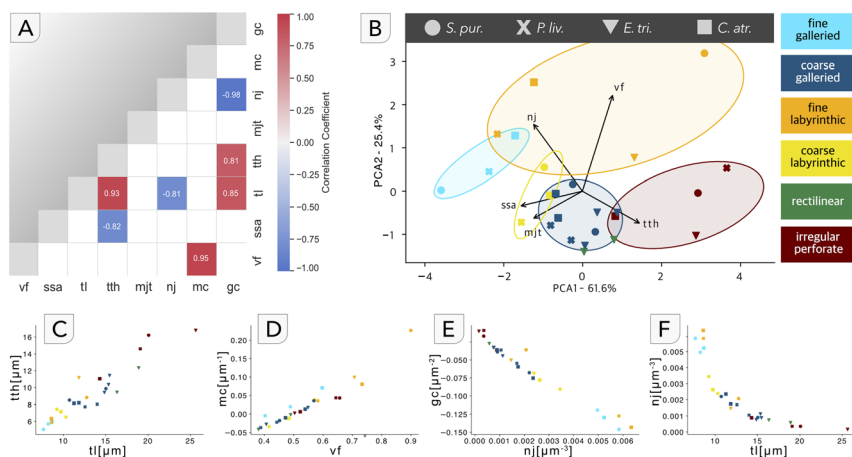

Fig. 5 (A) Matrix of correlation pairwise correlation coefficients for descriptors of the 6 major stereom subtypes found in the coronal plates of four species of sea urchins. vf: mineral volume fraction [a.u.]; ssa: specific surface area [m^2 cm^{-3}]; tth: mean trabecular thickness [µm]; tl: mean trabecular length [µm]; mjt: mean joint type as defined in the skan library; nj: number density of trabecular junctions [µm^{-3}]; mc: mean curvature [µm^{-1}]; gc: gaussian curvature [µm^{-2}]. (B) Biplot of principle component analysis of morphometric descriptors for 6 major stereom subtypes (cyan: fine galleried; blue: coarse galleried; orange: fine labyrinthic; yellow: coarse labyrinthic; green: rectilinear; red: irregular perforated) found in the coronal plates of four species of sea urchins (circle: *S. pur.*; cross: *P. liv.*; triangle: *E. tri.*; square: *C. atr.*). Loadings for the descriptors vf, ssa, tth, mjt, and nj are indicated (black arrows). The confidence ellipses are drawn with radii of 1.6 standard deviations and are shaded according to the color of the stereom subtype they represent. The associated scree plot is presented in Fig. SI3.† (C–F) Scatterplots of the strongly correlated descriptor pairs trabecular thickness and length (C), mean curvature and volume fraction (D), gaussian curvature and number density of trabecular junctions (E), and number density of trabecular junctions and mean trabecular length (F).

features of some stereom types. For example, the perforate stereom is charac-terized by a large trabecular thickness (tth) and a low density of nodes (nj). At the extreme opposite (*i.e.*, small tth and large nj), one finds the fine galleried stereom typically found in the boss. The fine labyrinthic stereom is generally characterized by a low porosity (large mineral volume fraction and small specific surface area). Also, the PCA analysis supports that both the galleried and the labyrinthic ster-eom structures comprise fine and coarser subtypes. Interestingly, the coarser and finer textures of the same stereom type do not cluster in regions of the PCA component plane (for example, fine and coarse galleried stereom clusters are separated by the coarse labyrinthic one).

Another interesting observation emerges from the analysis of the local mean curvature distribution of the different stereom types. Excluding the fine laby-rinthic stereom, most of the stereom polymorphs have a mean curvature close to zero (between -0.05 μm^{-1} and 0.05 μm^{-1}). Moreover, the standard deviation of the curvature distribution in the natural system is comparable to that of a computed constant-mean-curvature (CMC) surface (*e.g.*, Schwarz D) sampled using grid dimensions and with volume fractions comparable to those of our SR-μCT data (see Fig. SI4†).

Discussion

We report herein on a rapid and robust classification scheme for stereom struc-tures that draws on the power spectra of cubic sample volumes (edge length 65 μm). We further demonstrate that this scheme succeeds in differentiating ster-eom subtypes where the use of morphometric descriptors in combination with dimensionality reduction methods such as PCA fail. The large distance in the PCA map between the two galleried and the two labyrinthic stereom types, as well as the overlap between the different stereom types, suggests that the most important features of the sea urchin stereom, those that best capture the details of its polymorphism, are the distribution of orientations of the trabecular rods and their typical distances. These are not easy to capture in real space with simple morphometric descriptors, especially in a rotationally invariant way, but are the essence of the power spectrum and reflected in their specific symmetry.

Our results show that the anisotropic galleried stereom is oriented such that the main struts grow/point in all directions (*i.e.*, parallel as well as perpendicular to the plate surfaces), irrespective of the calcite lattice orientation. Moreover, we found that the fine galleried stereom exhibits very similar orientations, typical distances and morphometric descriptors in three of the four studied species. These observations clearly indicate that trabeculae can grow practically unconstrained in a large range of angular distributions, irrespective of the crystallographic directions. In contrast, growth of the spicules in sea urchin larvae and the spines in adult specimens is much faster in certain crystallographic directions than in others. In both spicule and spines, growth is thought to occur by addition of amorphous calcium carbonate precursor. We speculate that the ability of the adult sea urchin to grow single-crystalline calcitic structures independent of the lattice orientation is owed to kinetic control over mineral crystallisation.[48] Furthermore, the mature sea urchin calcite comprises around 10% amorphous material[17]. The presence of amorphous material could alleviate the accumulation of lattice strains that in turn may affect the direction of growth[48] or the development of stresses.[17] The echinoderms grow their

skeletal elements in a tightly confined space determined by the skeletogenic cells.[49–53] This may facilitate the cellular control of mineral morphogenesis and growth rates that override the effect of molecular contributions determined by mineral crystallographic orientation, contrary to observations in other biological systems.[48]

Interestingly, the diverse stereom polymorphs share a common property: they exhibit a mean curvature close to zero and a negative Gaussian curvature. These properties are also characteristic of triply periodic minimal surfaces (TPMSs), such as Schwarz diamond and Schwarz primitive (D and P) and the gyroid. The idea that the stereom of echinoderm plates can be described as minimal surfaces was first proposed by Donnan and Pawson in 1969 (ref. 7) and recently demonstrated in *Cidaris rugosa*[54] and *Protoreaster nodosus*.[55] Our results expand on this analysis and demonstrate that the sea urchin stereom can be described as a (periodic and non-periodic) structure of constant mean curvature. The observation that many of the structural descriptors fall on a common trend line (see Fig. 5C–F), regardless of stereom type and sea urchin species, suggests that the structural features of the stereom are widely interdependent. For periodic structures, such as the Schwarz P and D, the correlation between volume fraction and mean curvature at constant lattice size is well established.[56,57] Also, the linear correlation between trabecular length and thickness or the negative correlation between density of nodes and trabecular lengths at constant volume fraction simply results from the scaling of the periodic lattice. For the sea urchin stereom, however, these correlations appear independent of volume fraction, typical lengths, and periodicity, indicating that sea urchins may form CMC surfaces with a range of symmetries and organizational complexity unrelated to lattice scaling. Whether this may reflect functional, *e.g.*, mechanical, constraints or specific biophysical boundaries that are in place during the growth of the stereom remains to be determined.

Triply periodic minimal surfaces as well as related disordered constant-mean-curvature structures are found in nature, most commonly at the nanometric scale, for instance in block co-polymer and lipid mesophases, but also at the macroscopic scale, as in soap bubbles. Prominent examples in biology are structures formed by lipid membranes,[58] such as mitochondrial membranes of amoebas[59] and thylakoids of green algae.[60] Furthermore, the photonic structures found in some butterfly scales that are responsible for their bright coloration show similar symmetries and have been suggested to form by templating on a folded mould made of the endoplasmic reticulum and the plasma membranes.[61–63] Alternative models for the formation of TPMSs and related structures involve liquid–liquid phase separation of yet unknown components.[64,65] Another example of TPMS-based structural colours is found in bird feathers, which are thought to form through the phase separation of polymerizing β-keratin within the cytoplasm.[66] In contrast to these examples, which are all at the submicron scale, the characteristic length scale of the sea urchin stereom is significantly larger (hundreds of nanometers in the case of photonic structures and biological membranes *vs.* several to tens of microns in the stereom). This suggests distinct morphogenetic processes/mechanisms, adapted to different physical or chemical constraints at this larger scale, in the latter.

Curvature has been shown to act as a morphogenetic cue in multiple cellular systems, with minimization of the tissue surface tension leading to shapes of constant mean curvatures. We suggest that tension of the soft tissue in sea

urchins (stroma) also plays a critical role during stereom morphogenesis. Similar behaviour is observed in different cell cultures grown on substrates with varying curvature.[67] For example, it has been observed that osteoblast-cell cultures grown on saddle-shaped substrates (gaussian curvature <0) tend to develop into multi-layered tissue, where the mean curvature is minimized.[68] This behaviour was linked to cellular mechanosensing and implicated actin filament contraction (stress fibres) in the morphogenesis mechanism.[68–70] Finally, the secretion and distribution of cellular morphogenetic signals are often key factors in the formation of patterns in biology. These are usually described using models originally proposed by Turing,[71] in which the feedback between activator and inhibitor molecules in reaction–diffusion systems leads to complex patterns. In this context, it has been proposed that the occurrence of curvature could modulate the diffusion of the morphogens and/or their transport rates, suggesting a direct link between curvature and morphogenesis through a reaction–diffusion mechanism.[70] However, whereas these models are well-established in 2D systems, only a few studies address the problem in three dimensions.[72–75] Notably, it has been found that some triply-periodic minimal surfaces can be obtained using 3D Turing models for specific sets of parameters.[72] How these (3D Turing) models relate to the morphogenesis of sea urchin stereom polymorphs remains an open question.

Conclusions

Herein, we describe an approach to classifying stereom structure that is based on its 3D power spectrum rather than on discrete real-space measurements. Advantages of this approach include that it is unbiased, rapid, robust, rotationally invariant, and more representative of the 3D structure. We further show that all stereom structures we analysed possess constant mean curvature, but differ in pore volume fraction and symmetry.

We further find that the stereom symmetry is independent of the underlying crystallographic orientation of calcite and conclude that its structure likely reflects constraints imposed on the soft tissue that occupies the stereom pore space. The distribution of stereom polymorphs and their orientation within the test plate points towards a mechanical function. However, other factors, such as constraints from growth processes, the presence of living tissue, and the need to accommodate requirements like minimizing density, allowing transport, and facilitating cell motility, likely influence stereom morphology. More work is required to better understand the developmental processes that give rise to specific stereom polymorphs and the mechanisms that result in constant mean curvature at the micrometric scale. We anticipate that the analytical pipeline described herein will accelerate future comparison of stereom structure across different species and phylogenetic groups, and during skeletal development – as well as for the study of other complex 3D biomineral and biomaterial morphotypes.

Data availability

The data supporting this article have been included as part of the ESI.†

Author contributions

RS: conceptualization, investigation, methodology, formal analysis, data curation, software, visualization, writing – original draft, writing review and editing. KH: methodology, data curation, formal analysis, software, visualization, writing – review and editing. JP: investigation, methodology. DJ: writing – review and editing. MA: conceptualization, writing – review and editing. YP: conceptualization, writing – original draft, writing – review and editing, supervision, funding acquisition. LB: conceptualization, methodology, formal analysis, data curation, software, visualization, writing – original draft, supervision, writing – review and editing.

Conflicts of interest

There are no conflicts to declare.

Acknowledgements

Notes and references

1 D. M. Raup, *J. Geol.*, 1959, **67**, 661–674.
2 D. M. Raup, *Syst. Biol.*, 1962, **11**, 97–108.
3 D. M. Raup, *Memoir*, 1968, **2**, 50–63.
4 J. N. Weber, *Am. J. Sci.*, 1969, **267**, 537–566.
5 A. B. Smith, in *Special Papers in Palaeontology*, Palaeontological Association, 1980, vol. 25, pp. 1–81.
6 M. D. C. Carnevali, F. Bonasoro and G. Melone, *Boll. Zool.*, 1991, **58**, 1–42.
7 G. Donnay and D. L. Pawson, *Science*, 1969, **166**, 1147–1150.
8 S. Hyde, Z. Blum, T. Landh, S. Lidin, B. W. Ninham, S. Andersson and K. Larsson, *The Language of Shape: The Role of Curvature in Condensed Matter: Physics, Chemistry and Biology*, Elsevier Science, 1996.
9 B. M. Heatfield, *J. Exp. Zool.*, 1971, **178**, 233–246.
10 H.-U. Nissen, *Science*, 1969, **166**, 1150–1152.
11 J. Dafni, *Paleobiology*, 1986, **12**, 143–160.
12 A. B. Smith and C. W. Wright, *Monogr. Palaeontogr. Soc.*, 1990, **583**, 101–198.

13 O. Ellers and M. Telford, in *Echinoderms: San Francisco: Proceedings of the Ninth International Echinoderm Conference: San Francisco, California, USA, 5-9 August, 1996*, A. A. Balkema, Rotterdam, 1998.

14 E. Zolotoyabko, E. N. Caspi, J. S. Fieramosca, R. B. Von Dreele, F. Marin, G. Mor, L. Addadi, S. Weiner and Y. Politi, *Cryst. Growth Des.*, 2010, **10**, 1207–1214.

15 K. M. Towe, *Science*, 1967, **157**, 1048–1050.

16 S. J. Tsipursky and P. R. Buseck, *Am. Mineral.*, 1993, **78**, 775–781.

17 M. Albéric, E. N. Caspi, M. Bennet, W. Ajili, N. Nassif, T. Azaïs, A. Berner, P. Fratzl, E. Zolotoyabko, L. Bertinetti and Y. Politi, *Cryst. Growth Des.*, 2018, **18**, 2189–2201.

18 J. Seto, Y. Ma, S. A. Davis, F. Meldrum, A. Gourrier, Y.-Y. Kim, U. Schilde, M. Sztucki, M. Burghammer, S. Maltsev, C. Jäger and H. Cölfen, *Proc. Natl. Acad. Sci. U. S. A.*, 2012, **109**, 3699–3704.

19 I. Gordon, *Philos. Trans. R. Soc. London, Ser. B*, 1926, **214**, 259–312.

20 S. Kobayashi and J. Taki, *Calcif. Tissue Res.*, 1969, **4**, 210–223.

21 J. S. Pearse and V. B. Pearse, *Am. Zool.*, 1975, **15**, 731–751.

22 K. Märkel, *Zoomorphologie*, 1976, **84**, 279–299.

23 K. Märkel, *Zoomorphology*, 1981, **97**, 31–52.

24 J. D. Gage and P. A. Tyler, *Deep-Sea Biology: A Natural History of Organisms at the Deep-Sea Floor*, Cambridge University Press, Cambridge, 1991.

25 P. Gorzelak, A. Dery, P. Dubois and J. Stolarski, *Front. Zool.*, 2017, **14**, 42.

26 Y. Politi, T. Arad, E. Klein, S. Weiner and L. Addadi, *Science*, 2004, **306**, 1161–1164.

27 M. Albéric, C. A. Stifler, Z. Zou, C.-Y. Sun, C. E. Killian, S. Valencia, M.-A. Mawass, L. Bertinetti, P. U. P. A. Gilbert and Y. Politi, *J. Struct. Biol. X*, 2019, **1**, 100004.

28 E. Beniash, J. Aizenberg, L. Addadi and S. Weiner, *Proc. Biol. Sci.*, 1997, **264**, 461–465.

29 Y. Politi, R. A. Metzler, M. Abrecht, B. Gilbert, F. H. Wilt, I. Sagi, L. Addadi, S. Weiner and P. U. P. A. Gilbert, *Proc. Natl. Acad. Sci. U. S. A.*, 2008, **105**, 17362–17366.

30 Y. U. T. Gong, C. E. Killian, I. C. Olson, N. P. Appathurai, A. L. Amasino, M. C. Martin, L. J. Holt, F. H. Wilt and P. U. P. A. Gilbert, *Proc. Natl. Acad. Sci. U. S. A.*, 2012, **109**, 6088–6093.

31 C. C. Tester, C.-H. Wu, M. R. Krejci, L. Mueller, A. Park, B. Lai, S. Chen, C. Sun, M. Balasubramanian and D. Joester, *Adv. Funct. Mater.*, 2013, **23**, 4185–4194.

32 J. W. Durham and R. V. Melville, *J. Paleontol.*, 1957, **31**, 242–272.

33 A. B. Smith, *Philos. Trans. R. Soc. London, Ser. B*, 1980, **289**, 1–54.

34 J. N. Grossmann and J. H. Nebelsick, *Zoomorphology*, 2013, **132**, 301–315.

35 C. Lauer, T. B. Grun, I. Zutterkirch, R. Jemmali, J. H. Nebelsick and K. G. Nickel, *Zoomorphology*, 2018, **137**, 139–154.

36 H. Chen, T. Yang, Z. Wu, Z. Deng, Y. Zhu and L. Li, *Acta Biomater.*, 2020, **107**, 218–231.

37 T. Yang, Z. Wu, H. Chen, Y. Zhu and L. Li, *Acta Biomater.*, 2020, **107**, 204–217.

38 D. Müter, H. O. Sørensen, J. Oddershede, K. N. Dalby and S. L. S. Stipp, *Acta Biomater.*, 2015, **23**, 21–26.

39 T. B. Grun and J. H. Nebelsick, *R. Soc. Open Sci.*, 2018, **5**, 171323.

40 H. Yu, J. Li, Z. Hou, J. Li, Y. Chen and C. Lin, *J. Bionic Eng.*, 2020, **17**, 469–483.

41 J. Schindelin, I. Arganda-Carreras, E. Frise, V. Kaynig, M. Longair, T. Pietzsch, S. Preibisch, C. Rueden, S. Saalfeld, B. Schmid, J.-Y. Tinevez, D. J. White, V. Hartenstein, K. Eliceiri, P. Tomancak and A. Cardona, *Nat. Methods*, 2012, **9**, 676–682.

42 J. Nunez-Iglesias, A. J. Blanch, O. Looker, M. W. Dixon and L. Tilley, *PeerJ*, 2018, **6**, e4312.

43 L. Curcuraci, L. Bertinetti and A. Narkevicius, BMML tools **https://bmmltools.readthedocs.io/en/latest/**.

44 C. Esteves, C. Allen-Blanchette, A. Makadia and K. Daniilidis, *Int. J. Comput. Vis.*, 2020, **128**, 588–600.

45 H. Skibbe, Q. Wang, O. Ronneberger, H. Burkhardt and M. Reisert, in *2009 IEEE 12th International Conference on Computer Vision Workshops, ICCV Workshops*, IEEE, Kyoto, Japan, 2009, pp. 1863–1869.

46 V. Perricone, P. Cesarano, A. Mancosu, D. Asnicar, S. Bravi and F. Marmo, *J. R. Soc. Interface*, 2023, **20**, 20220673.

47 H. Chen, Z. Jia, Z. Deng and L. Li, *Extreme Mech. Lett.*, 2024, **68**, 102137.

48 V. Schoeppler, D. Stier, R. J. Best, C. Song, J. Turner, B. H. Savitzky, C. Ophus, M. A. Marcus, S. Zhao, K. Bustillo and I. Zlotnikov, *Adv. Mater.*, 2021, **33**, 2101358.

49 P. T. Johnson and F. A. Chapman, *J. Invertebr. Pathol.*, 1970, **16**, 116–122.

50 E. Kniprath, *Calcif. Tissue Res.*, 1974, **14**, 211–228.

51 K. Märkel, U. Röser, U. Mackenstedt and M. Klostermann, *Zoomorphology*, 1986, **106**, 232–243.

52 K. Okazaki, *Am. Zool.*, 1975, **15**, 567–581.

53 P. Dubois and L. Ameye, *Microsc. Res. Tech.*, 2001, **55**, 427–437.

54 A.-L. Jessop, A. J. Millsteed, J. J. K. Kirkensgaard, J. Shaw, P. L. Clode and G. E. Schröder-Turk, *J. R. Soc. Interface*, 2024, **21**, 20230597.

55 T. Yang, H. Chen, Z. Jia, Z. Deng, L. Chen, E. M. Peterman, J. C. Weaver and L. Li, *Science*, 2022, **375**, 647–652.

56 Y. Jung, K. T. Chu and S. Torquato, *J. Comput. Phys.*, 2007, **223**, 711–730.

57 D. M. Anderson, H. T. Davis, L. E. Scriven and J. C. C. Nitsche, in *Advances in Chemical Physics*, ed. I. Prigogine and S. A. Rice, Wiley, 1st edn, 1990, vol. 77, pp. 337–396.

58 Z. A. Almsherqi, S. D. Kohlwein and Y. Deng, *J. Cell Biol.*, 2006, **173**, 839–844.

59 Y. Deng and M. Mieczkowski, *Protoplasma*, 1998, **203**, 16–25.

60 T. Zhan, W. Lv and Y. Deng, *Protoplasma*, 2017, **254**, 1923–1930.

61 H. Ghiradella, *J. Morphol.*, 1989, **202**, 69–88.

62 H. T. Ghiradella and M. W. Butler, *J. R. Soc. Interface*, 2009, **6**, S243–S251.

63 V. Saranathan, C. O. Osuji, S. G. J. Mochrie, H. Noh, S. Narayanan, A. Sandy, E. R. Dufresne and R. O. Prum, *Proc. Natl. Acad. Sci. U. S. A.*, 2010, **107**, 11676–11681.

64 S. L. Burg, A. Washington, D. M. Coles, A. Bianco, D. McLoughlin, O. O. Mykhaylyk, J. Villanova, A. J. C. Dennison, C. J. Hill, P. Vukusic, S. Doak, S. J. Martin, M. Hutchings, S. R. Parnell, C. Vasilev, N. Clarke, A. J. Ryan, W. Furnass, M. Croucher, R. M. Dalgliesh, S. Prevost, R. Dattani, A. Parker, R. A. L. Jones, J. P. A. Fairclough and A. J. Parnell, *Commun. Chem.*, 2019, **2**, 1–10.

65 H. Ghiradella and W. Radigan, *J. Morphol.*, 1976, **150**, 279–297.

66 V. Saranathan, S. Narayanan, A. Sandy, E. R. Dufresne and R. O. Prum, *Proc. Natl. Acad. Sci. U. S. A.*, 2021, **118**, e2101357118.

67 S. J. P. Callens, R. J. C. Uyttendaele, L. E. Fratila-Apachitei and A. A. Zadpoor, *Biomaterials*, 2020, **232**, 119739.

68 S. Ehrig, B. Schamberger, C. M. Bidan, A. West, C. Jacobi, K. Lam, P. Kollmannsberger, A. Petersen, P. Tomancak, K. Kommareddy, F. D. Fischer, P. Fratzl and J. W. C. Dunlop, *Sci. Adv.*, 2019, **5**, eaav9394.

69 B. Schamberger, S. Ehrig, T. Dechat, S. Spitzer, C. M. Bidan, P. Fratzl, J. W. C. Dunlop and A. Roschger, *PNAS Nexus*, 2024, **3**, pgae121.

70 B. Schamberger, R. Ziege, K. Anselme, M. Ben Amar, M. Bykowski, A. P. G. Castro, A. Cipitria, R. A. Coles, R. Dimova, M. Eder, S. Ehrig, L. M. Escudero, M. E. Evans, P. R. Fernandes, P. Fratzl, L. Geris, N. Gierlinger, E. Hannezo, A. Iglič, J. J. K. Kirkensgaard, P. Kollmannsberger, Ł. Kowalewska, N. A. Kurniawan, I. Papantoniou, L. Pieuchot, T. H. V. Pires, L. D. Renner, A. O. Sageman-Furnas, G. E. Schröder-Turk, A. Sengupta, V. R. Sharma, A. Tagua, C. Tomba, X. Trepat, S. L. Waters, E. F. Yeo, A. Roschger, C. M. Bidan and J. W. C. Dunlop, *Adv. Mater.*, 2023, **35**, 2206110.

71 A. M. Turing, *Philos. Trans. R. Soc. London, Ser. B*, 1952, **237**, 37–72.

72 H. Shoji, K. Yamada, D. Ueyama and T. Ohta, *Phys. Rev. E: Stat., Nonlinear, Soft Matter Phys.*, 2007, **75**, 046212.

73 W. Song, F. Wubs, J. Thies and S. Baars, *Commun. Nonlinear Sci. Numer. Simulat.*, 2018, **60**, 145–164.

74 T. Leppänen, M. Karttunen, K. Kaski, R. A. Barrio and L. Zhang, *Phys. D*, 2002, **168–169**, 35–44.

75 T. K. Callahan and E. Knobloch, *Phys. D*, 1999, **132**, 339–362.